IEEE Robotics and Automation Letters (RA-L) paper, presented at ICRA 2026, Vienna, Austria. Cite as RA-L paper.

A Robotic System with Path Planning and Visual Guidance for Teleoperated Left Atrial Appendage Closure

Angela Peloso[1,*], Nadia D'Alessandro[2,*], Xiu Zhang[1], Arianna Menciassi[2] and Elena De Momi[1]

***Abstract*—Percutaneous Left Atrial Appendage Closure (LAAC) is a minimally invasive procedure to prevent thromboembolic events in atrial fibrillation patients. The procedure's success relies on precise navigation and occluder deployment, which is challenged by sheath movement in the dynamic cardiac environment, procedural complexity, and prolonged radiation exposure. This study introduces a robotic-assisted navigation system for LAAC procedure, integrating a dedicated steerable sheath, custom planning algorithms, and an intuitive teleoperation interface. The path-planning framework generates collision-free routes based on patient-specific anatomy, adjusting for deviations in real-time. The teleoperation interface comprises a digital replica of the patient's anatomy with real-time visual feedback to the user for precise and intuitive navigation. Bench-top validation demonstrated that navigation guidance reduced target position error by 2.03% with the planner and 2.85% with the replanner, compared to free navigation without planning assistance. Planning and replanning strategies also reduced collisions with cardiac structures, highlighting the platform's potential to improve procedural precision and safety.**

***Index Terms*—Medical Robots and Systems, Surgical Robotics: Steerable Catheters/Needles, Surgical Robotics: Planning, Telerobotics and Teleoperation.**

I. INTRODUCTION

The Left Atrial Appendage (LAA) is a small sac in the Left Atrium (LA) of the heart that aids blood storage and release. Despite its size, the LAA is a major risk factor for thromboembolic events, such as strokes, in patients with Atrial Fibrillation (AF). AF is the most common cardiac arrhythmia worldwide, affecting 2% to 4% of the population, with cases expected to double due to aging population [1]. Studies reveal that over 90% of blood clots in the heart originate in the LAA, highlighting its critical role in stroke prevention in AF [2].

Percutaneous closure of the LAA (i.e., LAAC) offers a minimally invasive alternative to long-term anticoagulation therapy for AF patients at high bleeding risk. This procedure involves advancing a Delivery Sheath (DS) from peripheral access in the femoral vein to the heart. After transseptal puncture, the DS is guided into the LAA, where an occlusion device is deployed to seal it (Fig. 1). Transesophageal echocardiography (TEE) and fluoroscopy provide real-time imaging for precise navigation and device placement. Procedural success depends on accurate deployment, yet peri-device leaks (PDLs) occur due to improper device sizing or positioning, increasing the thromboembolism risk [3]. Coaxial alignment of the DS with the LAA is crucial for an optimal implant, but the variability in LAA shapes and orientation, and the heart's dynamic environment make this task challenging [4]. While non-steerable DSs are the clinical standard, emerging steerable delivery sheaths (SDSs) promise greater maneuverability and adaptability [5]. Robotic systems are increasingly used in vascular and cardiac procedures, improving catheter control with respect to manual advancement, and reducing radiation exposure. Examples include CorPath GRX (Siemens Healthineers, Germany) for neurovascular interventions, Genesis RMN systems (Stereotaxis, USA) for cardiac ablation, R-One+ (Robocath, France) for coronary artery disease, and TAVI-PILOT (Caranx Medical, France) for valve implantation. However, robotic-assisted systems have never been employed for LAAC procedures. The use of robotic catheters introduces new challenges, particularly in navigating the constrained anatomical environment. Planning an optimal route through minimizing the risk of collisions is critical [6]–[8]. The inherent complexity and dynamics of the clinical scenario can lead to unexpected deviations from the planned path, necessitating the use of a replanner. Real-time surgical guidance ensures that the catheter remains on a safe trajectory, correcting its course as needed to maintain an

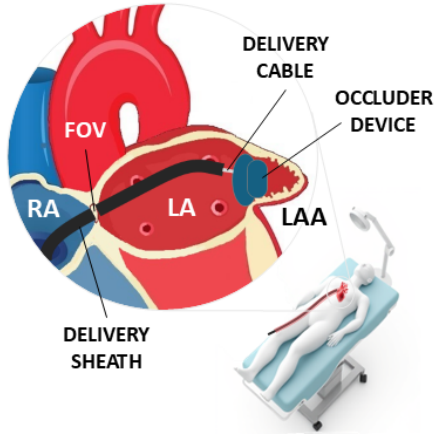

Fig. 1. LAAC procedure: a delivery sheath, a delivery cable, and an occluder device are shown. Heart structures: right atrium - RA, fossa ovalis - FOV, left atrium - LA, left atrial appendage - LAA.

Manuscript received: February 17, 2025; Revised: May 15, 2025; Accepted: July 4, 2025.

This paper was recommended for publication by Editor Pietro Valdastri upon evaluation of the Associate Editor and Reviewers' comments.

*These authors contributed equally.

[1] Angela Peloso, Xiu Zhang and Elena De Momi are with the Department of Electronics, Information, and Bioengineering, Politecnico di Milano, Italy angela.peloso@polimi.it

[2] Nadia D'Alessandro and Arianna Menciassi are with The BioRobotics Institute, Scuola Superiore Sant'Anna of Pisa, Italy nadia.dalessandro@santannapisa.it

Digital Object Identifier (DOI): see top of this page.

IEEE Robotics and Automation Letters (RA-L) paper, presented at ICRA 2026, Vienna, Austria. Cite as RA-L paper.

optimal path even in dynamic and unpredictable conditions.

This work presents, to the best of the authors' knowledge, the first integrated robotic platform for percutaneous LAAC interventions with real-time path planning and teleoperated guidance. The main contributions are:

1) Adaptive real-time navigation assistance for a SDS designed for LAAC procedure, leveraging a task-specific RRT* planning-replanning framework, with spline interpolation and patient-specific collision checking.
2) A teleoperation interface that delivers intuitive real-time control and visual feedback within a virtual anatomical environment.

The platform was validated in an in-vitro setup, with navigation trials performed with and without planning assistance, demonstrating improved targeting accuracy and reduced collisions when using guidance-assisted navigation compared to manual control.

II. Related work

Over the past decade, several SDSs for LAAC have emerged in preclinical studies and the market. Occlutech (Switzerland) developed an SDS capable of $180°$ bending, while LifeTech Scientific (China) proposed the FuStar SDS with a single deflectable curve up to $160°$. Abbott (USA) released the Amplatzer SDS, featuring a $45°$ proximal curve and a deflectable distal curve up to $120°$, though it was recalled in 2023 due to thromboembolism risks. Boston Scientific (USA) recently introduced the Watchman TrueSteer, offering bi-directional steering. Medtronic (USA) demonstrated the FlexCath Advance SDS with a bending curve up to $135°$ for implanting Watchman (Boston Scientific, USA) and Amulet (Abbott, USA) occluders [9]. Studies suggest SDSs improve procedural outcomes by enhancing coaxial alignment and reducing PDL incidence [9]–[11].

Commercial deflectable catheters are typically extruded polymer tubes reinforced with metal braids or coils for torque and kink resistance, a PTFE liner for lubricity, and pull tendons. Recent trends explore notched nitinol tubes designs, where selective material removal allows for customized curvature and stiffness. These structures are dexterous and precisely controllable. Haga et al. [12] used femtolaser-engraved nitinol tubes to create microscale bending catheters capable of $160°$ deflection. Bell et al. [13] demonstrated slotted nitinol catheters providing $180°$ deflection for MRI-guided interventions. Jeong et al. [14] developed the COAST robot with three coaxial nitinol tubes achieving variable curvatures.

With the rise of more dexterous catheters and robotic-assisted cardiac systems, planning algorithms play a crucial role in optimizing trajectories and avoiding obstacles, thus reducing tissue damage [15]. Planning methods can be broadly categorized [6] as graph-based or sampling-based. Graph-based algorithms, like Dijkstra's [16] and A* [17], discretize the environment to find efficient paths using heuristics. Xu et al. [18] developed a graphical interface for surgeons to define collision-free trajectories with A* algorithm on vascular maps. While effective in static and discrete environments, graph-based approaches struggle with real-time adaptability. Sampling-based algorithms, such as rapidly exploring random tree (RRT) and probabilistic roadmaps, incrementally explore the environment, making them ideal for high-dimensional, dynamic spaces with real-time replanning capabilities [19], [20]. A hybrid Bi-directional RRT approach [21], optimized with cubic Bezier splines, achieved smooth trajectories and a 90% success rate in steerable guidewire navigation. Fan et al. [22] combined RRT with a graph-based potential field algorithm for real-time replanning, while Li et al. [23] used breadth-first search and genetic algorithms to ensure safety in endovascular catheterization. Sampling-based algorithms have been validated in simulations and real-world scenarios. Kuntz et al. [24] demonstrated a backward RRT strategy [25] in porcine lung biopsy models, achieving target error accuracy of $1.8 – 3.4$ mm. Integrating planning algorithms into robotic systems has improved teleoperated catheter navigation, enhancing control and adaptability [26], [27]. For example, the open-source CardioXplorer system for atrial ablation [28] enabled joystick-based navigation with real-time feedback, resulting in smoother motion and reduced variability.

III. Robotic Sheath Design

A. LAAC system

The proposed LAAC system consists of three components: a SDS, a robotic steering module, and a robotic driver. The steerable sheath (Fig. 2-a) has an outer diameter (OD) of 8 mm and a working length of approximately 85 cm. It features a 10 cm nitinol notched tip mounted on a multi-lumen polymer tube using a custom PLA 3D printed connector. Inside the nitinol tube, a polyester braid sleeve (nominal diameter: 6 mm) confines tendons aside and prevents them from drifting. The tendons run between the sleeve and the nitinol, then through the polymer tube channels. The cross-section of the steerable sheath (section A-A) is shown in Fig. 2-b. The nitinol tip bends via tendon actuation and includes segments with varying stiffness, achieved through tailored notched patterns. These notches are created on a plain nitinol tube (OD: 8 mm, wall thickness: 0.37 mm, MeKo Manufacturing, Germany) using electrical discharge machining. The proximal segment, with eight asymmetric notches, bends in one direction in the medio-lateral plane (Fig. 3-a.1) via a single tendon, while the distal segment, with five notches, bends bidirectionally in both the medio-lateral (Fig. 3-a.2) and antero-posterior planes (Fig. 3-a.3) using two pairs of antagonistic tendons. The proximal and distal segments bend approximately 70° and 60°, respectively. Once combined, the sheath spans 6.65 cm in the medio-lateral plane and 2.95 cm in the antero-posterior plane. Anatomical studies by Maceira et al. [29] report the LA's transversal diameter as 4.1 ± 0.5 cm (four-chamber view), 4.6 ± 0.5 cm (two-chamber view), and an antero-posterior diameter of 3.2 ± 0.5 cm, suggesting the sheath's workspace can adequately cover the LA anatomy.

The robotic steering module (Fig. 3-b) controls the nitinol tip. It uses five independent linear actuators (Fig. 3-c), each driven by a brushless DC motor (Faulhaber 3242 G 024 BX4 CS) integrated with a 9:1 lead screw gearbox. The motor's rotation drives the linear movement of the nut along the lead screw. The actuators are arranged around the sheath, which is constrained radially and axially. Tendons exit laterally from

IEEE Robotics and Automation Letters (RA-L) paper, presented at ICRA 2026, Vienna, Austria. Cite as RA-L paper.

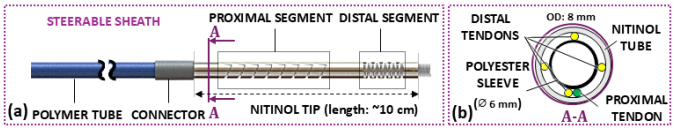

Fig. 2. a) The steerable sheath, comprising the polymer tube, the connector, the nitinol tip and the polyester sleeve. b) Cross-section (A-A, in purple).

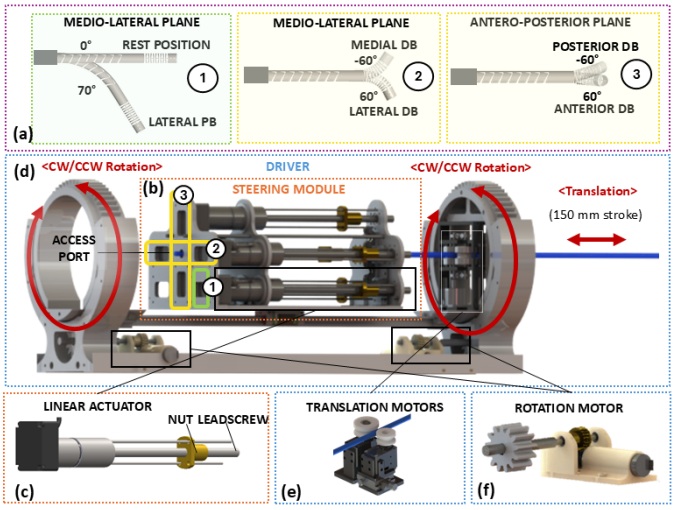

Fig. 3. a) Steering degrees of freedom of the nitinol tip: 1) proximal bending, 2) medio-lateral distal bending, and 3) antero-posterior distal bending. b) The steering module, consisting of five independent linear actuators. c) Mechanical components of the linear actuator. d) Robotic driver. e) Mechanical components of the translation mechanism. f) Mechanical components of the rotation mechanism.

the sheath channels, pass through a pulley stage, and connect to the nuts. As a nut retracts, it pulls the associated tendon, steering the tip. The back access port of the central working channel can be used to introduce the LAA occluder.

The robotic driver (Fig. 3-d) controls both the translation and rotation of the sheath [30]. Translation (Fig. 3-e) is achieved through two motors (XM430-W350-R, Dynamixel) rotating synchronously to drive a pair of silicone-coated wheels, that compress the sheath and push it forward. The steering module slides passively on a 500 mm linear rail, with a maximum stroke of 150 mm in the current design. Rotation (Fig. 3-f) is controlled by two motors (Faulhaber 2250S024BX4 CSD 3830), located posteriorly and anteriorly at the base of the driver. Each motor drives a worm screw that engages a two-stage gear. The synchronous motors' motion make the posterior and anterior big wheels rotate together in the same direction.

Motors receive input via serial communication from two workstations: one for the robotic driver and one for the steering module. These systems feature motion control with a position encoder. A wireless joystick (DualShock DS4, PS4, Sony) sends position commands (Fig. 4). The left side controls the driver: up/down arrows for translation, L1 and L2 for rotation. The right side controls the steering module: four buttons for anterior, posterior, medial, and lateral distal bending (DB), and R1 and R2 for proximal bending (PB) and release. The Robot Operating System (ROS) network processes joystick commands and sends them to the motor control firmware, while a LabVIEW program controls the steering motors.

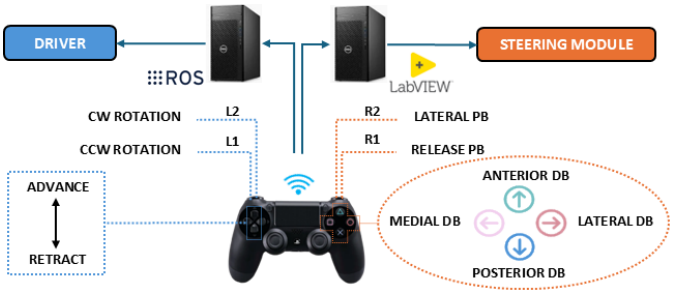

Fig. 4. Joystick commands and control flow. Abbreviations: PB: proximal bending; DB: distal bending; CW: clockwise; CCW: counter-clockwise.

B. Nitinol tip model

The sheath's nitinol tip ensures optimal co-axial alignment with the LAA, thanks to the combination of proximal and distal bending. With reference to Fig. 5, the nitinol tip features the following segments: $L_A = 7$ mm, $L_B = 15$ mm (bending), $L_C = 20$ mm, $L_D = 55$ mm (bending). In a 2D kinematic model, L_B and L_D are constant curvature arcs (Fig. 5).

The tip position $\boldsymbol{P}^G \in \mathbb{R}^3[x_G, y_G, z_G]$ in the global reference frame $\{G\}$ is obtained by multiplying the transformation matrices with $\boldsymbol{P}^A$ in the local reference frame $\{A\}$:

$$\begin{aligned}\boldsymbol{P}^G &= f(\alpha, \beta, L_A, L_B, L_C, L_D) \\ &= \boldsymbol{T}_D^G \cdot \boldsymbol{T}_C^D(\alpha) \cdot \boldsymbol{T}_B^C \cdot \boldsymbol{T}_A^B(\beta) \cdot \boldsymbol{P}^A \\ &= \begin{bmatrix} \boldsymbol{R}_D^G & \boldsymbol{t}_D^G \\ 0 & 1 \end{bmatrix} \cdot \begin{bmatrix} \boldsymbol{R}_C^D & \boldsymbol{t}_C^D \\ 0 & 1 \end{bmatrix} \cdot \begin{bmatrix} \boldsymbol{R}_B^C & \boldsymbol{t}_B^C \\ 0 & 1 \end{bmatrix} \cdot \begin{bmatrix} \boldsymbol{R}_A^B & \boldsymbol{t}_A^B \\ 0 & 1 \end{bmatrix} \cdot \begin{bmatrix} 0 \\ L_A \\ 0 \\ 1 \end{bmatrix}\end{aligned} \tag{1}$$

Rotation matrices represent 3D Euler rotation around z-axis and are given as: $\boldsymbol{R}_D^G = \boldsymbol{R}_z(-30°), \boldsymbol{R}_C^D = \boldsymbol{R}_z(\alpha), \boldsymbol{R}_B^C = \boldsymbol{R}_z(0), \boldsymbol{R}_A^B = \boldsymbol{R}_z(\beta)$. The reference frame $\{D\}$ is tilted by $-30°$ relative to the global reference frame $\{G\}$ to reflect the anatomical orientation of the to the heart's longitudinal axis with respect to the inferior vena cava [31]. Translation vectors are given by:

$$\begin{aligned} \boldsymbol{t}_D^G &= \begin{bmatrix} 0 \\ 0 \\ 0 \end{bmatrix} & \boldsymbol{t}_C^D &= \begin{bmatrix} \frac{L_D}{\alpha}(1 - \cos(\alpha)) \\ \frac{L_D}{\alpha}\sin(\alpha) \\ 0 \end{bmatrix} \\ \boldsymbol{t}_B^C &= \begin{bmatrix} 0 \\ L_C \\ 0 \end{bmatrix} & \boldsymbol{t}_A^B &= \begin{bmatrix} \frac{L_B}{\beta}(1 - \cos(\beta)) \\ \frac{L_B}{\beta}\sin(\beta) \\ 0 \end{bmatrix} \end{aligned} \tag{2}$$

IV. NAVIGATION

A. Path planning problem

The path planning problem aims at finding an optimal path inside the atrium chamber, ensuring an appropriate clearance from atrium walls. The space of robot's configurations (C_{space}) is divided into two distinct regions (Fig. 6-a): the occupied space (C_{obs}), representing atrium walls that must be avoided, and the free space (C_{free}) where the robot can navigate without interference. The entire path must lie on C_{free}, starting from an initial position ($\boldsymbol{P}^S \in \mathbb{R}^3$), located right after the septum, up to a target position ($\boldsymbol{P}^E \in \mathbb{R}^3$), manually placed in the center of the ostium of the LAA. The movement was characterized by only the position of the tip ($\boldsymbol{P}^G$), which was rendered as a tubular object of diameter 8 mm.

IEEE Robotics and Automation Letters (RA-L) paper, presented at ICRA 2026, Vienna, Austria. Cite as RA-L paper.

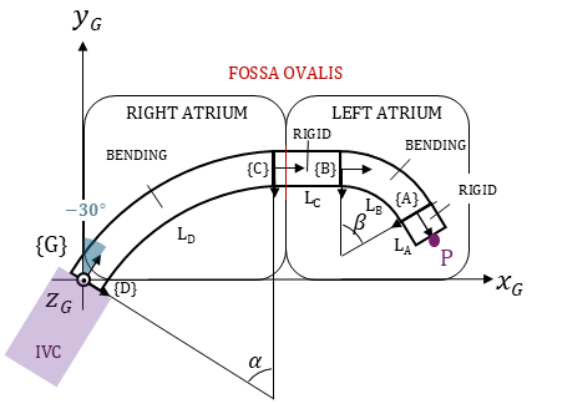

Fig. 5. Planar kinematic model of the nitinol tip. Point P denotes the distal end of the tip. The z-axis of all reference frames extends outward. Abbreviations: IVC - Inferior vena cava.

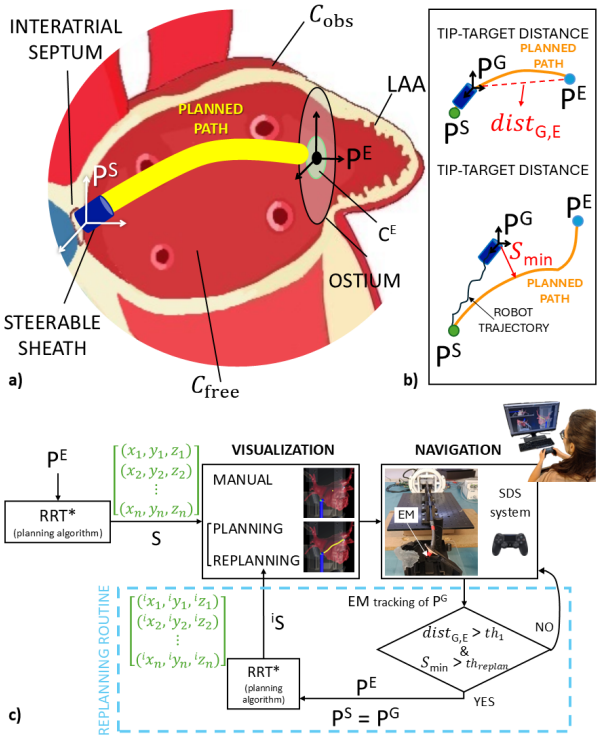

Fig. 6. Path planning problem setup: a) C_{obs} (atrium walls) and C_{free} (atrium chamber). The planned path (yellow line) goes from $\boldsymbol{P}^S$ to $\boldsymbol{P}^E$, located within a target area C^E (light green). b) Replanning conditions. c) Replanning strategy based on EM tracking.

B. Replanning logic

To generate a suitable path, RRT* [32] was employed. The RRT (Algorithm 1) incrementally expands a tree, T, from the starting position (line 1) to the target positions in a collision-free manner through random sampling of the task space. The algorithm samples random positions in the task space C_{free} (line 3), selects the nearest node in the tree (line 4), and attempts to extend the tree towards the sampled position (line 5). If the edge between these two nodes is free from obstacles (line 6), then the new node is added to the tree (line 12), with the nearest node as its parent (line 7). The RRT* enhances RRT by iteratively rewiring the tree to minimize overall cost (line $8-11$), here defined as the Euclidean distance between

Algorithm 1: RRT* Algorithm

1 **Tree Initialization** : $T \leftarrow \mathbf{P}^S$
2 $r = 1$
3 $N_{\text{rand}} \leftarrow$ `GetRandomNode`
4 $N_{\text{nearest}} \leftarrow$ `FindClosestNodeOnTree`(N_{rand})
5 $N_{\text{new}} \leftarrow$ `SteerFromNearestNode`
6 **if** $noCollision(N_{nearest}, N_{new})$ **then**
7 $\quad N_{\text{new}}.parent \leftarrow N_{\text{nearest}}$
8 $\quad N_{\text{new}}.cost \leftarrow N_{\text{nearest}}.cost + \|N_{\text{new}}, N_{\text{nearest}}\|$
9 $\quad nearestN \leftarrow$ `FindNearestNeighbors`(N_{new}, r)
10 $\quad$ **for** $N \in nearestN$ **do**
11 $\quad\quad$ `UpdateCost`(N_{new})
12 $\quad N_{\text{new}} \leftarrow T$
13 **if** $TargetReached$ **then**
14 $\quad$ `ComputeSpline` $\leftarrow S$

two nodes. Before adding a new node, nearby nodes within radius r are sequentially evaluated to identify the optimal parent with the lowest cost (i.e., the shortest Euclidean distance from the root node). The algorithm ends when the target is reached within 1 mm tolerance. A spline interpolation (S, line 14) is then computed using 5 five control points from the final path nodes in T.

After an initial path was computed, to enable replanning (Algorithm 2) the tip position P^G was continuously tracked in real-time (line 2). Replanning conditions (Fig. 6-b) were evaluated when the Euclidean distance ($dist_{\text{G-E}} = \|\boldsymbol{P}^E - \boldsymbol{P}^G\|$) between $\boldsymbol{P}^G$ and $\boldsymbol{P}^E$ exceeded a predefined threshold (th_1 - line 4). This approach avoided unnecessary calculations when the sheath was very close to the target, thereby reducing the overall computational load. Adherence to the planned path was assessed by sampling multiple points along the spline. The closest point to $\boldsymbol{P}^G$, characterized by the smallest Euclidean distance S_{min} (Fig. 6-b), was identified (line 5). If S_{min} exceeded th_{replan}, indicating significant deviation, replanning was triggered (line 6), with RRT* algorithm re-computing a new collision-free path from $\boldsymbol{P}^G$ to $\boldsymbol{P}^E$. The workflow is illustrated in Fig. 6-c.

Algorithm 2: Replanning

1 **if** $TargetReached$ **then**
2 $\quad$ **StartCoroutine** `CatheterPositionTracking`
3 **while** *true* **do**
4 $\quad$ **if** $dist_{G\text{-}E} > th_1$ **then**
5 $\quad\quad S_{\text{min}} \leftarrow min(\|\mathbf{P}^{\boldsymbol{G}}, S\|)$
6 $\quad\quad$ **if** $S_{min} > th_{replan}$ **then**
7 $\quad\quad\quad$ **Replanner** $\rightarrow$ `RRT* Algorithm`

V. Experimental Protocol

A. Setup and Calibration

A virtual replica of the patient's anatomy was created using a computed tomography (CT) scan of a candidate for LAAC at Ospedale San Raffaele in Milan, Italy, collected under ARTERY project. Key cardiac structures were delineated using 3DSlicer software [33] and subsequently imported into Unity (version 2022.3) [34] as 3D mesh models. The virtual anatomical environment represents the virtual domain for path planning and navigation. It uses a static anatomic model due to severely impaired contractility [35] and is consistent with current clinical practice, where route planning is based on preoperative CT scans [36].

IEEE Robotics and Automation Letters (RA-L) paper, presented at ICRA 2026, Vienna, Austria. Cite as RA-L paper.

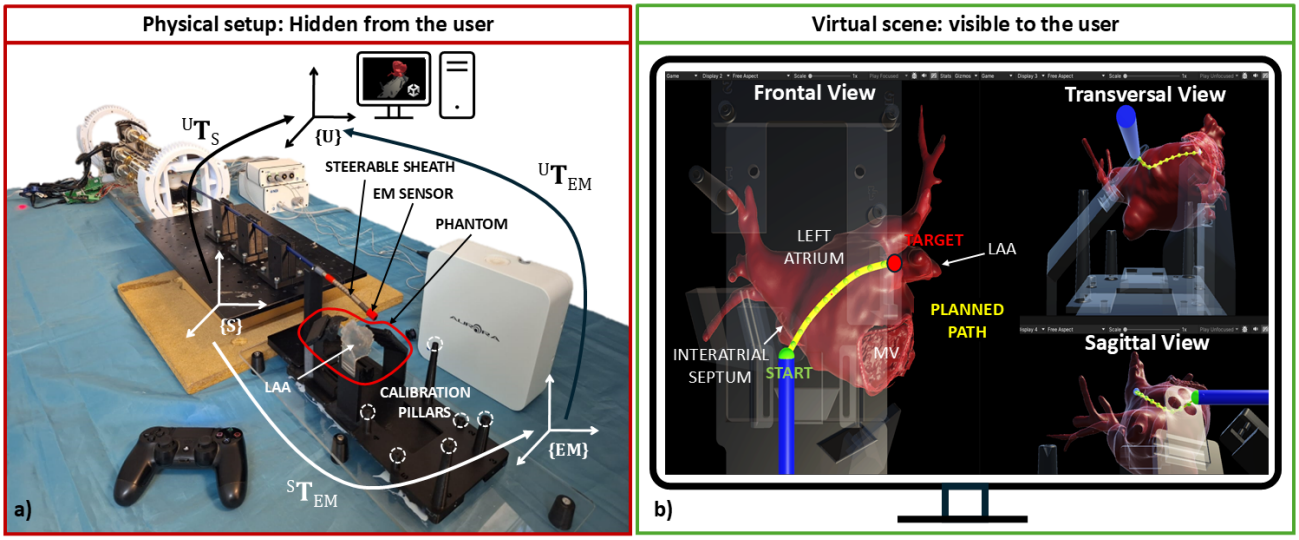

Fig. 7. a) Physical experimental setup, hidden from the user: the robotic SDS with an EM sensor at its tip, a 3D-printed phantom, an EM field generator and calibration pillars; b) User interface in Unity simulation environment with frontal, transversal and sagittal views.

The experimental setup (Fig. 7-a) included the physical hardware, hidden from the user, and a virtual scene displayed on a screen. The hardware comprised the SDS integrated with the steering module and the driver, a 3D-printed phantom, and an electromagnetic (EM) field generator (Aurora, NDI, USA). A 6 DoF EM sensor (0.92 x 9.4 mm) attached on the sheath's distal tip streamed position data at 40 Hz for real-time monitoring. The phantom, derived from the same CT scan, included an interatrial septum with a silicone pre-punctured fossa ovalis and a mitral valve (black), both 3D printed using PLA, and a LAA made of flexible silicone-like resin (Flexible 80A, FormLabs, USA) to mimic soft tissue (transparent).

The static phantom included reference pillars for calibration [37], ensuring the alignment between physical S and virtual U domains. The SDS was aligned with the fossa ovalis entry point using PLA support structures. The virtual scene (Fig. 7-b) displayed the LA, the sheath's initial position and the trajectory. Frontal, transverse, and sagittal views offered a comprehensive visualization of the sheath position relative to the anatomy.

B. Navigation task protocol

An experimental study was conducted to evaluate the teleoperated robotic platform and path-following performance, involving three users aged 26 to 28 with engineering backgrounds. Before testing, participants practiced for ten minutes using a PS4 joystick to control the sheath's movements while observing the physical system's response. During testing, users teleoperated the sheath from the fossa ovalis to the LAA under three conditions (Fig. 7-c):

- (*manual*): users navigated in the virtual environment without path assistance;
- (*planner*): a pre-computed spline path, displayed in Unity, guided navigation without adapting to real-time sheath deviations;
- (*replanner*): a dynamic replanner adapted the path when significant deviations were recorded.

In all three cases, users relied solely on the virtual scene for vision, as the physical setup was hidden from the user. The SDS tip's position, tracked by the EM sensor, was always displayed in real time. Each user performed three randomized trials per condition (27 in total). The replanning frequency was 0.2 Hz. The replanning was triggered when thresholds on $dist_{\text{G-E}}$ and S_{min} were satisfied. The threshold th_1 was set to 7 mm to prevent trajectory updates once the catheter tip entered the LAA landing zone (10-12 mm from the ostium [38]) with the rigid distal sheath segment; beyond this point, further replanning risks generating unstable or non executable paths in a confined space. Therefore, *replanner* was disabled, reducing computational overhead. The threshold th_{replan} was set to 4 mm based on preliminary manual navigation trials in simulation: we tested 2 mm, 4 mm, and 7 mm over three runs each, recording the total number of replanning events and the median path deviation (d_{path}, see Section V-C). A 2 mm threshold improved accuracy by only < 0.3 mm while increasing replans by over 50%, whereas a 7 mm threshold yielded median deviations above 5 mm. Thus, 4 mm provided the best trade off between stability and accuracy.

No limit to replanning attempts was imposed. The position of the target was made to vary within 1 mm around in x-y-z directions at each new navigation trial, covering the whole target area C^E. The actuation parameters of the robotic system, including the rotation, translation and steering velocity, and the resolution of steering increments were preset and remained constant throughout testing. After each trial, the sheath was reset to its initial position.

C. Performance metrics

The following global metrics were collected for the three navigation conditions:

- Target Position Error (TPE [mm]): final position error of the SDS tip upon reaching the target, measured as the Euclidean distance between $\boldsymbol{P}^E$ and the calibrated $\boldsymbol{P}^G$, (TPE $= \|\boldsymbol{P}^E - \boldsymbol{P}^G\|$), when a collision event was recorded between the target and sheath tip meshes;
- SDS path length (L_{SDS} [mm]): total path length traveled by the sheath, computed as the sum of the Euclidean distances between consecutive tracked tip positions:

IEEE Robotics and Automation Letters (RA-L) paper, presented at ICRA 2026, Vienna, Austria. Cite as RA-L paper.

$$L_{\text{SDS}} = \sum_{k=1}^{N} \|\boldsymbol{P}^{G_{\text{k}}} - \boldsymbol{P}^{G_{\text{k-1}}}\| \tag{3}$$

where N is the number of EM-tracked positions;

- Total planning time (t_{SDS} [s]): total navigation time from a starting position to the reaching of the target;
- $N_{\text{collision}}$: total collision events between $\boldsymbol{P}^G$ and the atrium wall mesh in the virtual environment.

To assess replanning, specific metrics were considered:

- Tracking Error (TE [mm]): Minimum distance between $\boldsymbol{P}^G$ and the planned spline ${}^iS$, triggering replanning routine when exceeding the threshold.
- Replanning time ($t_{\text{replanning}}$ [s]): time to replan a new obstacle-free path.
- Deviation from the planned path (d_{path} [mm]): Euclidean distance of $\boldsymbol{P}^G$ trajectory (downsampled at 100 points) from the planned route:

$$\text{d}_{\text{path}} = \|\boldsymbol{P}_j^G - S_j\|,\ j = 1..100 \tag{4}$$

with $S = {}^0S$ in *planner* condition, and $S = {}^iS$ in *replanner* condition.

- Replanning event position (REP [-]): normalized cumulative distance (0=start, 1=final point before th_1) indicating where along the trajectory a replanning event occurs.

Statistical analysis was conducted in Matlab to extract median and interquartile ranges (IQR). Non-parametric Mann-Whitney U test was performed to assess the statistical significance.

VI. Platform Validation and Discussion

Metrics' results are reported in Table I and in Fig. 8. The length of the traveled path L_{SDS} was lowest in the *manual* condition, while both *planner* and *replanner* conditions resulted in longer trajectories, although not statistically significant. Similarly, the total travel time (t_{SDS}) was lowest in the *manual* condition, followed by the *planner* (not significant) and the *replanner* condition (significantly higher, p-value = 0.0086). These findings can be attributed to the behavior observed under guidance, where the presence of a suggested path encouraged users to frequently adjust their trajectory. These repeated corrections contributed to deviations and increased both the total traveled distance and the overall travel time. However, this aligns with the system's design priorities, which emphasize adaptive path refinement and collision avoidance over rapid navigation. The TPE exhibited a progressive median reduction from the *manual* to the *replanner* condition (2.03% decrease with *planner* and a 2.85% decrease with *replanner*). This trend suggests that the replanning strategy enhanced placement accuracy, ensuring a more controlled approach to target localization. Furthermore, the number of collisions ($N_{\text{collision}}$) decreased in both the *planner* and *replanner* conditions compared to *manual* navigation, indicating that structured guidance mechanisms help mitigate erratic movements and reduce unintended contact with anatomical structures. While not statistically significant, these trends highlight the potential of assisted guidance to enhance procedural stability and safety. The system's real-time responsiveness was demonstrated by the TE metric, which showed that the *replanner* consistently kept the sheath within a narrow deviation threshold (median 5.52 mm), minimizing excessive divergence from the intended path (25^{th} percentile = 4.45 mm; 75^{th} percentile = 7.39 mm).

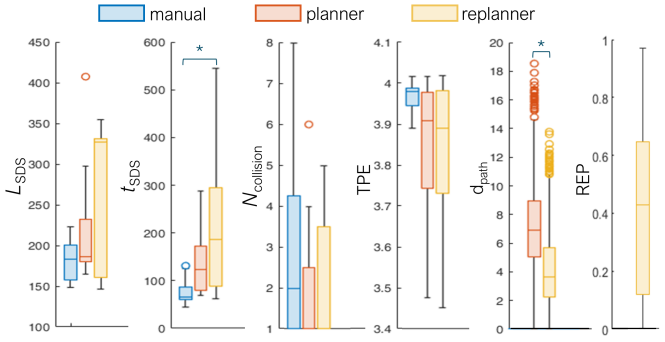

Fig. 8. Statistical analysis of performance metrics (L_{SDS} [mm], t_{SDS} [s], TPE [mm], $N_{\text{collision}}$, d_{path} [mm], REP[-]). Stars indicate statistical significance (p-value<0.05) while horizontal brackets connect the methods being compared.

The d_{path} metric demonstrated a significant improvement in trajectory adherence with the *replanner* system compared to the *planner*, with users deviating much less from the intended path (median d_{path} = 3.62 mm; IQR = 3.41 mm) than with the standard approach (median = 6.91 mm; IQR = 3.88 mm, $p < 0.05$). This suggests that by dynamically correcting early deviations, the *replanner* kept users on track and allowed the final portion of the path to be executed with greater accuracy, thereby compensating for user control limitations and reducing the impact of manual inaccuracies during navigation. Further evidence of the *replanner*'s supportive role is seen in the distribution of replanning events (REP metric): most interventions occurred in the first half of the trajectory (median normalized position = 0.43; IQR = 0.53), indicating that users initially struggled with the suggested route, but they gradually improved. Moreover, the replanning time ($t_{\text{replanning}}$), with a median of 1.27 s and an IQR of 0.42 s, highlighted the system's ability to quickly compute updated, obstacle-free paths, making it suitable for real-time intraoperative use. Future studies should incorporate a complementary assessment to better characterize how replanning guidance supports users, capturing aspects of subjective operator confidence and experience, not fully reflected in quantitative metrics.

	Manual		**Planner**		**Replanner**	
	Median	**IQR**	**Median**	**IQR**	**Median**	**IQR**
L_{SDS} **[mm]**	189.99	44.17	195.36	74.60	326.72	159.41
t_{SDS} **[s]**	67.07	42.80	122.47	84.68	236.88	238.48
TPE [mm]	2.46	0.04	2.41	0.23	2.39	0.18
$N_{\text{collision}}$	2	3.5	1	2.5	1	3.5

TABLE I
STATISTICAL ANALYSIS - MEDIAN AND IQR.

To provide a qualitative assessment, Fig. 9 illustrates the step-by-step progression of a navigation trial, showing the sheath's movement from the starting position to the target. The upper row captures the user display with real-time EM tracking of the sheath tip. In parallel, the bottom row highlights the corresponding physical SDS movements, including manipulations such as advancing, rotating, proximal (PB) and distal (DB) parts bending. On the right, a representative trajectory of the SDS is shown in 3D space. For the *manual* condition, the sheath's movement (cyan line) is represented as it progresses from the starting point (green) to the last recorded path point (red) and finally approaches the target (blue). The distance

IEEE Robotics and Automation Letters (RA-L) paper, presented at ICRA 2026, Vienna, Austria. Cite as RA-L paper.

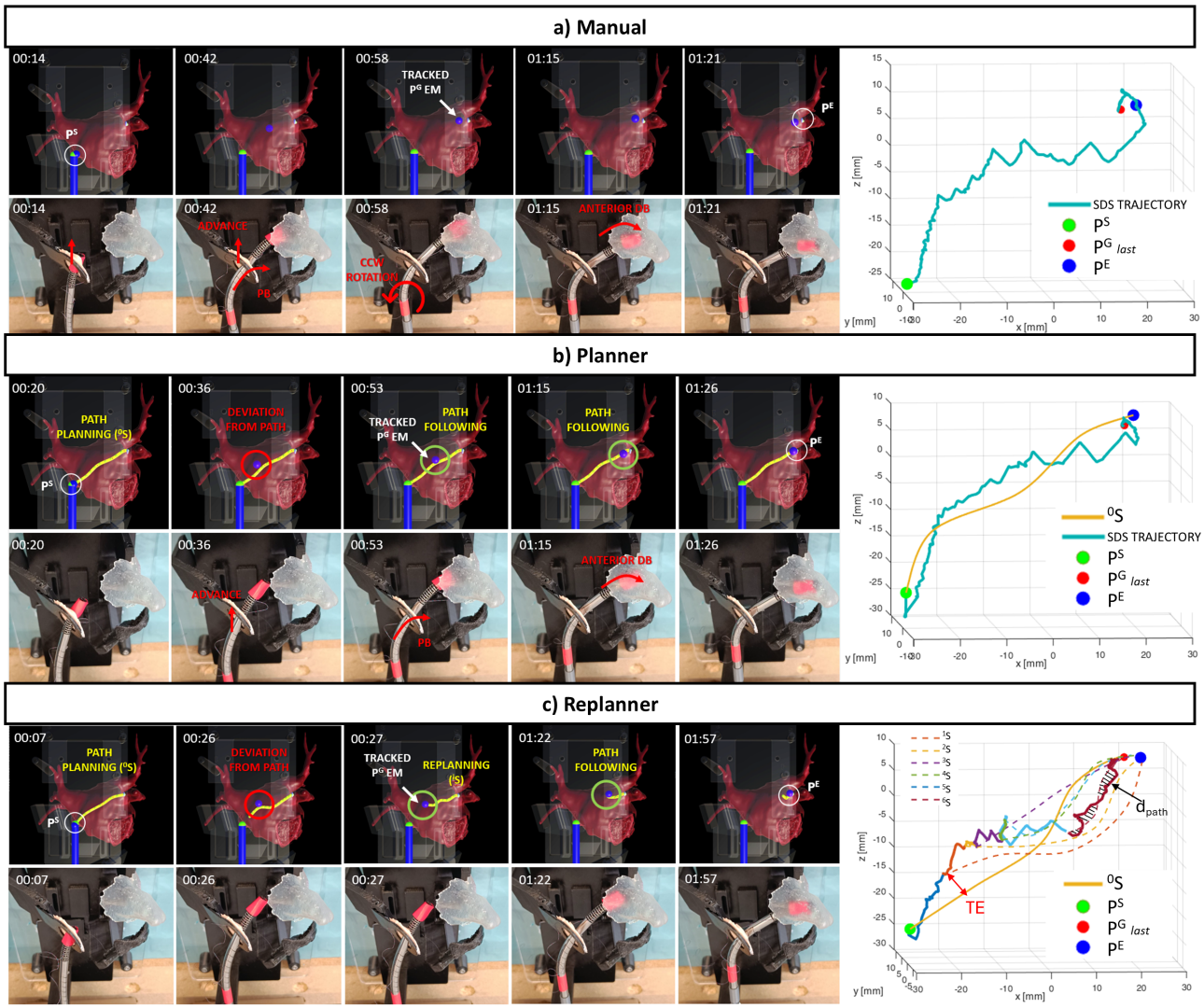

Fig. 9. Time instants in the user display (upper row) and physical system (bottom row) in the three conditions (a, b, c). On the right side, collected data of the SDS trajectory (blue line - a *manual*) from $\mathbf{P}^S$ to $\mathbf{P}^E$, with ${}^0S$ (orange line -b *planning*) and ${}^iS$ (dashed lines - c *replanner*). $\mathbf{P}^G last$ is the last tracked tip position when the collision is detected. TE between SDS trajectory and ${}^iS$ triggering replanning. d_{path} point-to-point between SDS trajectory and ${}^iS$. CCW: counterclockwise.

between the last recorded point and the target point accounts for the mesh thickness in the virtual environment, set at 3 mm. In the *planner* section, the initially planned path (orange spline) is also reported. In the *replanner*, the paths traveled by the SDS are represented with their suggested paths (dashed lines). For example, in the trial reported in Fig. 9-c, the user needed six replanning attempts before reaching the target.

VII. Conclusion

This work demonstrated an adaptive real-time navigation assistance module for a steerable LAAC sheath, paired with a teleoperation interface for live control and immersive anatomical visualization. The sheath includes a notched nitinol tip with two bending segments. Bending, translation, and rotation are fully motorized to enable precise and controlled navigation. The platform incorporates a patient-specific digital replica, providing real-time visualization of the sheath within anatomical structures relevant to LAAC. This system allows both path planning and dynamic replanning, suggesting sheath's guidance from the interatrial septum to the LAA while minimizing collisions and deviations. The platform validation involved three users navigating the sheath using a wireless joystick in three scenarios: manual navigation, planner-assisted navigation, and replanner-assisted navigation. Performance metrics were extracted using a workflow developed for accuracy and safety evaluation. Although *planner* and *replanner* modes increased path lengths and navigation times, the system showed adaptive path refinement capabilities and collision avoidance. The replanner condition improved accuracy, reducing errors and collisions, highlighting its potential to enhance safety and provide an alternative to fluoroscopy and TEE. Future improvements will refine path-planning algorithms to include sheath kinematics and further enhance system performance. This study establishes a foundation for larger cohort investigations to validate clinical impact and usability.

References

[1] G. Hindricks, T. Potpara, N. Dagres, E. Arbelo, J. J. Bax, C. Blomström-Lundqvist, G. Boriani, M. Castella, G.-A. Dan, P. E. Dilaveris, L. Fauchier, G. Filippatos, J. M. Kalman, M. La Meir, D. A. Lane, J.-P. Lebeau, M. Lettino, G. Y. H. Lip, F. J. Pinto, G. N. Thomas,

IEEE Robotics and Automation Letters (RA-L) paper, presented at ICRA 2026, Vienna, Austria. Cite as RA-L paper.

M. Valgimigli, I. C. Van Gelder, B. P. Van Putte, C. L. Watkins, and E. S. D. Group, "2020 ESC Guidelines for the diagnosis and management of atrial fibrillation developed in collaboration with the European Association for Cardio-Thoracic Surgery (EACTS)," *European Heart Journal*, vol. 42, no. 5, pp. 373–498, 08 2020.

[2] M. Święczkowski, E. J. Dąbrowski, P. Muszyński, P. Pogorzelski, P. Jemielita, J. M. Dudzik, T. Januszko, M. Duzinkiewicz, M. Południewski, Kuźma, M. Kożuch, P. Kralisz, and S. Dobrzycki, "A comprehensive review of percutaneous and surgical left atrial appendage occlusion," *Journal of Cardiovascular Development and Disease*, vol. 11, no. 8, 2024.

[3] M. Alkhouli, C. R. Ellis, M. Daniels, M. Coylewright, J. E. Nielsen-Kudsk, and D. R. Holmes, "Left atrial appendage occlusion: current advances and remaining challenges," *JACC: Advances*, vol. 1, no. 5, p. 100136, 2022.

[4] M. Sonya Joy, M. Horst Sievert, M. Stefan Bertog, and M. Timothy Betts, "Left atrial appendage morphology in patients with nonvalvular atrial fibrillation," *Journal of Structural Heart Disease*, vol. 3, no. 1, pp. 8–14, 2017.

[5] S. U. Khan and S. S. Goel, ""steering" toward complete left atrial appendage closure," *Journal of the Society for Cardiovascular Angiography & Interventions*, vol. 3, no. 4, 2024.

[6] A. Pore, Z. Li, D. Dall'Alba, A. Hernansanz, E. De Momi, A. Menciassi, A. C. Gelpi, J. Dankelman, P. Fiorini, and E. Vander Poorten, "Autonomous navigation for robot-assisted intraluminal and endovascular procedures: A systematic review," *IEEE Transactions on Robotics*, vol. 39, no. 4, pp. 2529–2548, 2023.

[7] A. Segato, M. Di Marzo, S. Zucchelli, S. Galvan, R. Secoli, and E. De Momi, "Inverse reinforcement learning intra-operative path planning for steerable needle," *IEEE Transactions on Biomedical Engineering*, vol. 69, no. 6, pp. 1995–2005, 2021.

[8] A. Peloso, R. Damiano, X. Zhang, A. Bicchi, E. Votta, and E. De Momi, "Imitation learning for path planning in cardiac percutaneous interventions," *IEEE Transactions on Biomedical Engineering*, 2025.

[9] S.-N. Chang, F.-C. Chiu, J.-J. Chen, P.-S. Huang, T.-T. Lin, H.-L. Cheng, C.-F. Tsai, Y.-C. Wang, and C.-T. Tsai, "First-in-human experience of using a universal steerable sheath in implanting left atrial appendage closure devices," *JACC: Asia*, vol. 2, no. 6, pp. 780–783, 2022.

[10] N. Amabile, A. Belfekih, V. Balmette, K. Mahmoudi, N. Mignot, and C. Roig, "Steerable delivery sheath for left atrial appendage closure in patients with severely enlarged left atria," *Journal of the Society for Cardiovascular Angiography & Interventions*, vol. 3, no. 4, 2024.

[11] S. Maiani, G. Nardi, F. Ristalli, C. Di Mario, and F. Meucci, "Use of a steerable delivery sheath to obtain coaxial alignment in left atrial appendage occlusion after mitral transcatheter edge-to-edge repair: a case report," *European Heart Journal-Case Reports*, vol. 8, no. 1, 2024.

[12] Y. Haga, Y. Muyari, S. Goto, T. Matsunaga, and M. Esashi, "Development of minimally invasive medical tools using laser processing on cylindrical substrates," *Electrical Engineering in Japan*, vol. 176, no. 1, pp. 65–74, 2011.

[13] J. A. Bell, C. E. Saikus, K. Ratnayaka, V. Wu, M. Sonmez, A. Z. Faranesh, J. H. Colyer, R. J. Lederman, and O. Kocaturk, "A deflectable guiding catheter for real-time mri-guided interventions," *Journal of Magnetic Resonance Imaging*, vol. 35, no. 4, pp. 908–915, 2012.

[14] S. Jeong, Y. Chitalia, and J. P. Desai, "Design, modeling, and control of a coaxially aligned steerable (coast) guidewire robot," *IEEE Robotics and Automation Letters*, vol. 5, no. 3, pp. 4947–4954, 2020.

[15] B. Ren, Y. Zhao, J. Zhang, H. Li, K. Li, and J. Zhang, "The critical technologies of vascular interventional robotic catheterization: A review," *IEEE Sensors Journal*, vol. 23, no. 24, pp. 30 051–30 069, 2023.

[16] H. Liu, Y.-L. Fu, Y.-Y. Zhou, H.-X. Li, Z.-G. Liang, and S.-G. Wang, "An in vitro investigation of image-guided steerable catheter navigation," *Proceedings of the Institution of Mechanical Engineers, Part H: Journal of Engineering in Medicine*, vol. 224, no. 8, pp. 945–954, 2010.

[17] P. E. Hart, N. J. Nilsson, and B. Raphael, "A formal basis for the heuristic determination of minimum cost paths," *IEEE Transactions on Systems Science and Cybernetics*, vol. 4, no. 2, pp. 100–107, 1968.

[18] H. Xu, S. Guo, C. Li, and S. Cao, "Study on the path planning based on a* algorithm for vascular intervention robots," in *2024 IEEE International Conference on Mechatronics and Automation (ICMA)*, 2024, pp. 1610–1615.

[19] Y. Wang and Y. Chen, "Quasi-static path planning for continuum robots by sampling on implicit manifold," in *2024 IEEE International Conference on Robotics and Automation (ICRA)*. IEEE, 2024, pp. 8728–8734.

[20] G. Gao, D. Li, K. Liu, Y. Ge, and C. Song, "A study on path-planning algorithm for a multi-section continuum robot in confined multi-obstacle environments," *Robotica*, p. 1–24, 2024.

[21] J. Fauser, M. Fuchs, A. Ghazy, B. Dorweiler, and A. Mukhopadhyay, "Preoperative planning for guidewires employing shape-regularized segmentation and optimized trajectories," in *OR 2.0 Context-Aware Operating Theaters and Machine Learning in Clinical Neuroimaging: Second International Workshop Shenzhen, China, 2019, Proceedings 2*. Springer, 2019, pp. 12–20.

[22] Q. Fan, G. Cui, Z. Zhao, and J. Shen, "Obstacle avoidance for microrobots in simulated vascular environment based on combined path planning," *IEEE Robotics and Automation Letters*, vol. 7, no. 4, pp. 9794–9801, 2022.

[23] Z. Li, J. Dankelman, and E. De Momi, "Path planning for endovascular catheterization under curvature constraints via two-phase searching approach," *International Journal of Computer Assisted Radiology and Surgery*, vol. 16, pp. 619–627, 2021.

[24] A. Kuntz, M. Emerson, T. E. Ertop, I. Fried, M. Fu, J. Hoelscher, M. Rox, J. Akulian, E. A. Gillaspie, Y. Z. Lee, F. Maldonado, R. J. Webster, and R. Alterovitz, "Autonomous medical needle steering in vivo," *Science Robotics*, vol. 8, no. 82, p. eadf7614, 2023.

[25] J. Hoelscher, M. Fu, I. Fried, M. Emerson, T. E. Ertop, M. Rox, A. Kuntz, J. A. Akulian, R. J. Webster III, and R. Alterovitz, "Backward planning for a multi-stage steerable needle lung robot," *IEEE robotics and automation letters*, vol. 6, no. 2, pp. 3987–3994, 2021.

[26] R. Qi, N. U. Nayar, and J. P. Desai, "Compact design and task space control of a robotic transcatheter delivery system for mitral valve implant," *IEEE Transactions on Medical Robotics and Bionics*, vol. 5, no. 4, pp. 867–878, 2023.

[27] Y. Li, W. Wang, W. Duan, O. Olatunji Mumini, T. Akinyemi, W. Du, and Y. Zheng, "Design of vascular interventional surgical robot with network time delay analysis for master-slave teleoperation," in *2021 4th International Conference on Intelligent Autonomous Systems (ICoIAS)*, 2021, pp. 406–412.

[28] Z. Xu, A. M. Zeidan, Y. He, L. Leung, C. Byrne, S. Sabu, Y. Wu, Z. Chen, S. E. Williams, L. Lindenroth, J. Behar, C. A. Rinaldi, J. Whitaker, A. Arujuna, R. Housden, and K. Rhode, "Cardioxplorer: An open-source modular teleoperative robotic catheter ablation system," *Robotics*, vol. 13, no. 5, 2024.

[29] A. M. Maceira, J. Cosín-Sales, M. Roughton, S. K. Prasad, and D. J. Pennell, "Reference left atrial dimensions and volumes by steady state free precession cardiovascular magnetic resonance," *Journal of cardiovascular magnetic resonance*, vol. 12, no. 1, p. 65, 2010.

[30] X. Zhang, I. Tamadon, B. I. F. Jara, V. Cannizzaro, A. Peloso, A. Bicchi, A. Aliverti, E. Votta, A. Menciassi, and E. De Momi, "Design and hysteresis compensation of a telerobotic system for transesophageal echocardiography," *IEEE Robotics and Automation Letters*, 2024.

[31] B. Bulwer and J. Rivero, *Echocardiography pocket guide: the transthoracic examination*. Jones & Bartlett Learning, 2010.

[32] S. Karaman and E. Frazzoli, "Sampling-based algorithms for optimal motion planning," *The international journal of robotics research*, vol. 30, no. 7, pp. 846–894, 2011.

[33] A. Fedorov, R. Beichel, J. Kalpathy-Cramer, J. Finet, J.-C. Fillion-Robin, S. Pujol, C. Bauer, D. Jennings, F. Fennessy, M. Sonka, J. Buatti, S. Aylward, J. V. Miller, S. Pieper, and R. Kikinis, "3d slicer," 2024, software. [Online]. Available: https://www.slicer.org/

[34] Unity Technologies, "Unity," 2022, software. [Online]. Available: https://unity.com/

[35] P. Reynolds, "Cardiac arrhythmias and conduction disturbances," *Geriatric Rehabilitation Manual*, p. 265, 2007.

[36] M. Święczkowski, E. J. Dąbrowski, P. Muszyński, P. Pogorzelski, P. Jemielita, J. M. Dudzik, T. Januszko, M. Duzinkiewicz, M. Południewski, Ł. Kuźma *et al.*, "A comprehensive review of percutaneous and surgical left atrial appendage occlusion," *Journal of Cardiovascular Development and Disease*, vol. 11, no. 8, p. 234, 2024.

[37] X. Zhang, M. C. Palumbo, F. Perico, M. Magro, A. Fortuna, T. Magni, E. Votta, A. Segato, and E. D. Momi, "Robotic actuation and control of a catheter for structural intervention cardiology," in *2022 IEEE/RSJ International Conference on Intelligent Robots and Systems (IROS)*, 2022, pp. 5907–5913.

[38] U.S. Food and Drug Administration, "Summary of Safety and Effectiveness Data (SSED) for Amplatzer™ Amulet™ Left Atrial Appendage Occluder," U.S. Food and Drug Administration, Tech. Rep. P200049, August 2021.